International Journal Of
Industrial Electronics Control and Optimization
Print ISSN: 3517-2645
Online ISSN: 3568-2645
Homepage: https://ieco.usb.ac.ir/

A Novel Cascade Control Strategy for Robust Fuel Cell Systems Using Variable Gain Sliding Technique

Violet Farhad[1] | Seyed Mehdi Mirhosseini-Alizamini[2]

Department of Mathematics, Payame Noor University (PNU), Tehran, Iran[1-2]
Corresponding author's email: m_mihosseini@pnu.ac.ir

Article Info

Article type:
Research Article

Article history:
Received: 23-April-2025
Received in revised form: 23-June-2025
Accepted: 18-July-2025
Published online: 22-June-2026

Keywords:
PEM fuel cell,
Oxygen excess ratio,
Variable gain super-twisting algorithm,
Lyapunov stability analysis,
Cascade structure.

ABSTRACT

This paper introduces a new application of variable gain sliding mode control (VGST) to the air supply system of a proton exchange membrane fuel cell (PEMFC), which is crucial for its performance and longevity. The air supply system comprises a centrifugal compressor, a DC-DC converter, and a fuel cell stack, forming a complex and nonlinear system with multiple inputs and outputs. The VGST method adjusts the control gain based on the system state and the sliding level and employs a cascade structure to regulate the excess oxygen ratio and the compressor airflow. The main goals of VGST are to control the PEMFC output voltage and power under various load conditions and uncertainties and to optimize the excess oxygen ratio (λ_{O_2}) to avoid oxygen depletion and membrane damage. The stability and robustness of the proposed controller are verified by Lyapunov theory and its performance is superior compared to other controllers such as variable gain closed-loop control and constant gain sliding mode control (single loop and cascade). The controller is validated by simulation and experimental data and demonstrates that it can enhance the efficiency and reliability of the PEMFC system. The variable gain controller of the cascade structure was also tested under noisy and uncertain conditions to further confirm its desired performance and showed that it could cope well with adverse situations and achieve the control objectives.

I. Introduction

Fuel cells are electrochemical devices that convert the chemical energy of a fuel and an oxidant into electrical energy, with high efficiency and low emissions [1]. Among different types of fuel cells, proton exchange membrane fuel cells (PEMFCs) are widely used for various applications, such as electric vehicles, portable devices, and stationary power generation [2]. However, PEMFCs have some challenges, such as nonlinear dynamics, uncertain parameters, and varying load conditions that affect their performance and durability [3]. Therefore, effective control strategies are needed to regulate the output voltage and power of PEMFCs under different operating scenarios.

A crucial Proton Exchange Membrane Fuel Cell (PEMFC) subsystem is the air-feed system, which supplies pressurized air to the cathode side of the fuel cell stack. This system comprises a centrifugal compressor, a DC-DC converter, and the fuel cell stack, creating a complex nonlinear system with multiple inputs and outputs. Effective management of the air-feed system is essential for maintaining the oxygen excess ratio (λ_{O_2}) at an optimal level, which is a key parameter affecting the performance and lifespan of the PEMFC. The λ_{O_2} is defined as the ratio between the actual and the stoichiometric oxygen flow rates, and it should be kept between 2 and 3 to prevent oxygen starvation and membrane degradation [4]. However, the λ_{O_2} is affected by the load variations, the compressor dynamics, the converter efficiency, and the fuel cell characteristics, which introduce uncertainties, and nonlinearities in the system [5].

In recent years, many control strategies have been proposed to regulate the performance of polymer electrolyte membrane fuel cells, each with its specific objective. These include pressure differential control, compressor motor control, net output power control, and air stoichiometry ratio control, as well as sensor reduction [6], among others. One of the promising control techniques for the air-feed system is sliding mode control (SMC), which is a robust nonlinear control method that can handle uncertainties, disturbances,

and model mismatch [7]. SMC works by driving the system state to a predefined sliding surface and keeping it there by applying a discontinuous control input. However, SMC has some drawbacks, such as chattering, high control effort, and sensitivity to noise [8]. To address these limitations, Variable Gain Sliding Mode Control (VGSMC) has been introduced. This modified version of SMC adjusts the control gain based on the system state and the sliding surface [9]. To comprehensive study of sliding mode controllers, interested readers may refer to [10-16], to name a few.

In 2012, Gonzalez [17], implemented variable gain control method on spring-mass system by providing a new technique for measuring the noise bounds. They compared three classic Super Twisting Algorithm, variable gain STA and first order sliding mode and after implementation of these systems, they found out that the first order sliding mode control had little chattering and it was significantly decreased by both STA algorithm including the variable gain and the constant gain. Also the result showed that compared to the classic STA, the STA variable gain was able to compensate for the larger class of perturbation and to reduce the chattering in a higher degree. The authors in [5] have presented the management and control strategies of a distributed generation system powered by a PEM fuel cell. The aim of their control strategy is to reduce the current and voltage oscillations of the fuel cell and improve its lifetime. Aguiar et al. have compared two control strategies: one with the direct control of the fuel flow and another with the management of an energy storage system. The experimental results show that the second strategy can achieve better performance and stability. Chen et al. [18] proposed strategies utilizing second-order sliding mode control to achieve improved transient response during rapid stack changes. They introduced a second-order sliding mode control law based on a nonlinear optimization method to mitigate chattering, stabilize excess oxygen levels, and address the optimization problem of net power in fuel cells. The authors also suggested a cascade configuration with a super-twisting algorithm to enhance net power output by maintaining oxygen stoichiometry between 2 and 2.4 and employed a reduced three-state model for controller design.

The adoption of a cascade control architecture (outer loop: oxygen excess ratio λ_{O2}; inner loop: air flow rate) is grounded in recent advancements in fuel cell system optimization. As demonstrated by Kart et al. [19], this hierarchical structure—when integrated with intelligent techniques like fuzzy-PID coordination—reduces steady-state error and accelerates dynamic response under load current step changes, significantly outperforming single-loop configurations. Crucially, the decoupled loop design effectively isolates disturbance propagation: empirical data from Du et al. [20] confirms the superiority of cascade systems in disturbance rejection (e.g., pressure fluctuations, temperature spikes) compared to centralized multivariable controllers. Furthermore, thermodynamic stability analysis by Luo et al. [21] validates that staged control inherently mitigates oscillation risk under aggressive disturbances—addressing instability concerns in our design. This synergy of precision, robustness, and computational efficiency makes cascade control uniquely suited for proton exchange membrane fuel cell (PEMFC) applications. In 2018 [22] and in 2022 [23], Mirrashid et al. have used the VGSMC method to optimize fuel cell system and upper limb rehabilitees robot, achieving desirable results such as robustness against various internal and external disturbances, model uncertainties, and precision in tuning, regulation, and tracking of variables with finite-time convergence. Furthermore, by comparing VGSMC with standard sliding mode strategies, it was found that mechanical stresses are minimized (preventing mechanical wear), and chattering in the output is significantly reduced.

Incremona et al. in 2020 [24] introduces a general framework for the design and tuning of higher order sliding mode controllers with switched and variable gain. The framework can accommodate any order sliding mode controller and both continuous and discrete variation of the controller parameters. The authors have analyzed the properties of the closed-loop system and demonstrate the method on some examples of switched and variable gain higher order sliding mode controllers. In 2021 Ma et al. [25] have presented an adaptive variable gain sliding mode control method for a class of uncertain nonlinear systems. The method can estimate the system uncertainties and adjust the controller gain accordingly. They have proved the finite-time convergence and stability of the proposed method and have showed its superiority over the conventional sliding mode control and the fixed gain sliding mode control.

Tang et al. in 2022 [7] have investigated a cascade control strategy of sliding mode and PID for the air supply system of a PEM fuel cell. The authors have developed an expansion state observer to estimate the cathode pressure and reconstruct the oxygen excess ratio. The simulation results demonstrate that the proposed method has a faster response time and less overshoot than other methods.

Moré et al. [26] have presented the development of multiple input/multiple output sliding mode controllers for a fuel cell-super capacitor module in hybrid generation applications. The objective is to satisfy the demand and regulate the DC bus voltage, even in the presence of model uncertainties and varying operating conditions. The authors have used two design approaches: variable-gains first-order sliding mode and super-twisting second-order sliding mode control. The stability of the nonlinear controlled system is formally analyzed and the performance of the proposed controllers is compared with classic linear PID controllers.

This paper develops a nonlinear dynamic model of a PEM fuel cell. Traditional sliding mode control (SMC) induces chattering and high-frequency switching due to the sign

function in the control signal or instability. To resolve this, a high-order sliding mode (HOSM) control is proposed, ensuring stability, robustness, and chattering suppression. While the standard super-twisting algorithm (STA) with fixed gains fails to compensate for severe nonlinearities and large perturbations in the fuel cell system, this work introduces a variable-gain STA (VGST). The VGST adapts gains online to disturbances, reducing chattering while guaranteeing finite-time convergence, robustness, and stability. Crucially, the proposed continuous control law maintains accurate and robust stability under all conditions—unlike discontinuous alternatives. Time-varying gains further accelerate convergence and relax the need for precise perturbation bounds. Stability is proven via a quadratic Lyapunov function, and convergence time is analytically estimated. Beyond these contributions, this work breaks new ground by implementing the variable-gain controller within a cascaded architecture - a novel departure from existing literature. The cascaded implementation demonstrates three key operational advantages: substantial reduction of power fluctuations, enhanced stability against dynamic disturbances, and improved robustness to parametric uncertainties when compared to traditional single-loop configurations. These advancements are particularly valuable for practical fuel cell applications where system reliability and dynamic response are critical.

The rest of the paper is organized as follows. Section 2 is devoted to the dynamic modeling of a fuel cell system. Section 3 deals with a variable gain controller design based on Lyapunov stability and Section 4 is related to the design of the cascaded controller. The simulation results are given in Section 5. Finally, section 6 concludes the paper.

II. The fuel cell system dynamics model

The Fig. 1 shows the structure of the fuel cell system, which consists of the stack and its peripheral equipment. The model used in this study is based on the reference [27], but with some modifications. Instead of using tabular data to describe the relationship between some system states, the model uses continuous equations to interpolate the values between the data points. This eliminates the need for table lookup and simplifies the model. Following RakhtAla & Eini [28] and Tang et al. [29], properly validated continuous interpolation functions can maintain sufficient accuracy while offering computational advantages. Moreover, our choice of pressure over mass as state variables (as suggested by Oladosu et al. [30].) provides direct correlation with measurable quantities in real systems, simplifies physical interpretation, and yields more controller-friendly state equations. The model proposed in this study is a nonlinear dynamic model with six states: $X = \left[\omega_{cp}, P_{sm}, m_{sm}, P_{O_2}, P_{N_2}, P_{rm}\right]^T$. The states represent the compressor speed (ω_{cp}), the supply manifold pressure (P_{sm}), the supply manifold mass (m_{sm}), the oxygen partial pressure (P_{O_2}), the nitrogen partial pressure (P_{N_2}), and the return manifold pressure (P_{rm}). The model assumes that the air is composed of only oxygen and nitrogen, with 21% oxygen and 79% nitrogen by volume.

The dynamic model of the fuel cell is a mathematical representation of the behavior of the fuel cell over time, taking into account the physical and chemical processes that occur inside the fuel cell. There are different types of dynamic models for fuel cells, depending on the level of detail, the type of fuel cell, and the purpose of the model. Table 1 presents the states and their definitions for better understanding

Table 1. States and their definitions.

States	Descriptions
$\mathbf{x_1 = \omega_{cp}}$ **(rad/s)**	Motor angular speed
$\mathbf{x_2 = P_{sm}}$ **(atm)**	Supply manifold pressure
$\mathbf{x_3 = m_{sm}}$ **(kg)**	Air mass in the supply manifold
$\mathbf{x_4 = P_{O_2}}$ **(atm)**	Oxygen pressure at cathode side
$\mathbf{x_5 = P_{N_2}}$ **(atm)**	Nitrogen pressure at cathode side
$\mathbf{x_6 = P_{rm}}$ **(atm)**	Return manifold pressure

The dynamic model of the fuel cell considered in the paper is:

$$\dot{x}_1 = \frac{\eta_{cm}}{J_{cp}}\frac{k_t}{R_{cm}}(v_{cm} - k_v x_1) - \frac{C_p}{J_{cp}}\frac{T_{atm}}{\eta_{cp}}\left(\left(\frac{x_2}{P_{atm}}\right)^{\frac{\gamma-1}{\gamma}} - 1\right)\frac{W_{cp}}{x_1}, \tag{1}$$

$$\dot{x}_2 = \frac{\gamma R_a}{V_{sm}}\left(-K_{sm,out}x_2 + K_{sm,out}P_{v,ca} + K_{sm,out}\frac{x_5}{M_{N2}} + K_{sm,out}\frac{x_4}{M_{O2}}\right)\frac{\gamma x_2}{x_3} + W_{cp}\left(T_{atm} + \frac{T_{atm}}{\eta_{cp}}\left(\left(\frac{x_2}{P_{atm}}\right)^{\frac{\gamma-1}{\gamma}} - 1\right)\right), \tag{2}$$

$$\dot{x}_3 = W_{cp} - K_{sm,out}x_2 + K_{sm,out}P_{v,ca} + K_{sm,out}\frac{x_5}{M_{N2}} + K_{sm,out}\frac{x_4}{M_{O2}}, \tag{3}$$

$$\dot{x}_4 = -\frac{x_4}{m_{O2} + m_{N2} + \frac{P_{v,ca}V_{ca}M_v}{R_v T_{st}}} \times K_{ca,out}\left(-x_6 + P_{v,ca} + \frac{x_5}{M_{N2}} + \frac{x_4}{M_{O2}}\right) + y_{O2,in}K_{sm,out}\frac{(R_{O_2}T_{st})}{V_{ca}} \times \left(x_2 - \frac{x_4}{M_{O2}} - P_{v,ca} - \frac{x_5}{M_{N2}}\right) - n\frac{(R_{O_2}T_{st})}{V_{ca}}\frac{M_{O2}}{4F}I_{st}, \tag{4}$$

$$\dot{x}_5 = (1 - X_{O_2})(1 + \Omega_{atm})^{-1}K_{sm,out} \times \frac{R_{N2}T_{st}}{V_{ca}}\left(x_2 - \frac{x_4}{M_{O2}} - \frac{x_5}{M_{N2}} - P_{v,ca}\right) - \frac{x_5}{m_{O2} + m_{N2} + \frac{P_{v,ca}V_{ca}M_v}{R_v T_{st}}}K_{ca,out} \times \left(-x_6 + \frac{x_4}{M_{O2}} + \frac{x_5}{M_{N2}} + P_{v,ca}\right), \tag{5}$$

$$\dot{x}_6 = \frac{R_a T_{rm}}{V_{rm}} \times \left(K_{ca,out}\left(\frac{x_4}{M_{O2}} + \frac{x_5}{M_{N2}} + P_{v,ca} - x_6\right) - \left(P_{a_6}x_6^5 + P_{a_5}x_6^4 + P_{a_4}x_6^3 + P_{a_3}x_6^2 + P_{a_2}x_6 + P_{a_1}\right)\right). \quad (6)$$

The model uses the compressor motor voltage ($u=V_{cm}$ (V)) as the input control variable, and the fuel cell stack current ($d=I_{st}$ (A)) as the measured disturbance variable. The model parameters are given in Appendix A. The compressor air flow rate (W_{cp}) is a function of x_1, and x_2 [27].

The output voltage of the fuel cell depends on the stack current, the partial pressure of the reactants, the temperature of the fuel cell, and the humidity of the membrane. The output voltage is lower than the standard potential of the fuel cell due to various losses, such as ohmic losses, activation losses, and concentration losses. These losses are nonlinear functions of the fuel cell current, temperature, pressure, and chemical reactions. The thermodynamic potential, E, is given by the Nernst equation in its extended form.

$$E = N\left(E_0 + \frac{R\,T}{2\,F}\left\{\frac{P_{H2}\left(\frac{P_{02}}{P_{OP}}\right)^{\frac{0}{5}}}{P_{H_2O_C}}\right\}\right) \quad (7)$$

So, it can be written:

$$v_{cell} = E - v_{act} - v_{ohm} - v_{conc}, \quad (8)$$

$$v_{stack} = N\ v_{cell}, \quad (9)$$

$$P_{net} = P_{Stack} - P_{auxiliary}. \quad (10)$$

where symbols and parameters are given in Appendix A. Eq. (12) shows that the requested current (I_{st}) depends on the air flow $W_{o2,reacted}$, which causes a significant decrease in λ_{O_2}. As λ_{O_2} increases, the partial pressure of oxygen and the stack voltage (P_{st}) also increase. However, increasing λ_{O_2} also increases the compressor power demand and the losses. Therefore, the inlet air flow needs to be regulated and adjusted to match λ_{O_2} with the load variations. This is the main objective of the control system design.

$$\lambda_{O_2} = \frac{\text{Oxygen Supplied}}{\text{Oxygen reacted}} = \frac{W_{O2,in}}{W_{o2,reacted}}, \quad (11)$$

where

$$W_{o2,reacted} = M_{o2}\frac{n.I_{st}}{4.F}, \quad (12)$$

$$W_{O2,in} = X_{O_2,in}\frac{1}{(1+\Omega_{atm})}K_{sm,out} \times \left(x_2 - \frac{x_4}{M_{O2}}\frac{R_{O2}T_{st}}{V_{ca}} - \frac{x_5}{M_{N2}}\frac{R_{N2}T_{st}}{V_{ca}} - P_{v,ca}\right). \quad (13)$$

The polarization curve shows how the voltage and current of a fuel cell are related. The model of the polarization curve includes the ideal voltage and the different voltage drops in the fuel cell. The voltage drops are caused by activation, ohmic, and concentration effects. Fig. 2 illustrates how the fuel cell voltage decreases as the current increases because of these effects. (N_{cell}=260).

III. Lyapunov-Based Design of Variable Gain Super Twisting Algorithm for PEM Fuel Cell

This section proposes a Lyapunov function for designing a variable gain super twisting algorithm for PEM fuel cell. This design can be applied to the system with relative degree one. The oxygen excess ratio in the closed loop system converges in finite time, even with model uncertainty. The adaptive controller gains ensure robust regulation of the oxygen excess ratio despite severe uncertainty. The control signal is smooth and continuous, and the convergence time is bounded.

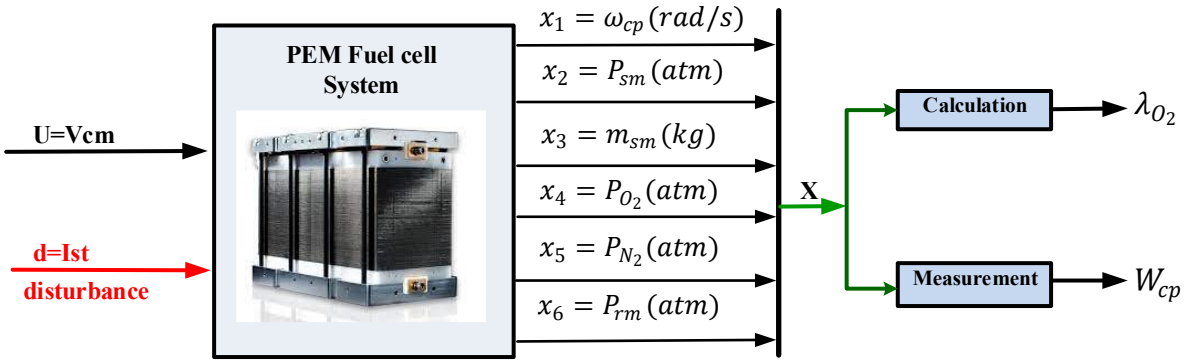

Fig. 1. Block diagram of the fuel cell system with state representation.

where x and $u = v_{cm}$ are the system states and control input, respectively, f and g are the unknown functions, and $d(t) = I_{st}$ indicates external perturbation and uncertainty of system parameters.

Before presenting the main finding of the paper, the following concept must be defined.

Definition 1. The sliding surfaces $s_1(t)$ and $s_2(t)$ are functions of the errors, $e_1(t)$, and $e_2(t)$, which $e_1(t)$ and $e_2(t)$ are the deviations of oxygen stoichiometry and compressor air flow from their desired value, respectively. The sliding surface $s_1(t)$ can be expressed as:

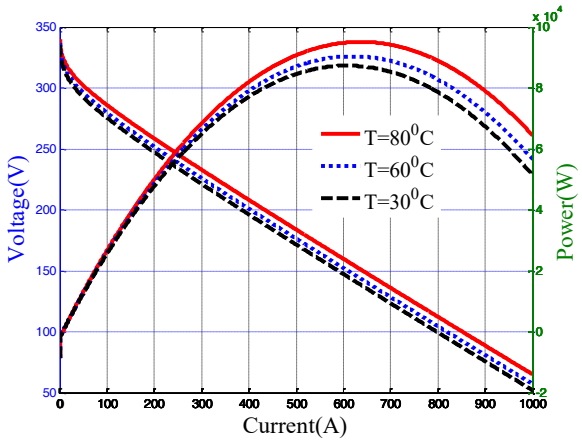

Fig. 2. Fuel cell characteristics for various values of temperature.

A dynamic model of the system can be expressed as follows:

$$\dot{x} = \begin{bmatrix} \dot{x}_1 \\ \dot{x}_2 \\ \dot{x}_3 \\ \dot{x}_4 \\ \dot{x}_5 \\ \dot{x}_6 \end{bmatrix} = f(x,t) + g(x,t)u + \varphi(x,t)d(t)\,, \tag{14}$$

with

$$f(x,t) = \begin{bmatrix} f_1(x_1, x_2) \\ f_2(x_1, x_2, x_3, x_4, x_5) \\ f_3(x_2, x_4, x_5) \\ f_4(x_2, x_4, x_5, x_6) \\ f_5(x_2, x_4, x_5, x_6) \\ f_6(x_4, x_5, x_6) \end{bmatrix}, \tag{15}$$

$$g(x,t) = \begin{bmatrix} \eta_{cm} \dfrac{k_t}{J_{cp} R_{cm}} \\ 0 \\ 0 \\ 0 \\ 0 \\ 0 \end{bmatrix},$$

$$\varphi(x,t) = \begin{bmatrix} 0 \\ 0 \\ 0 \\ -n \dfrac{M_{O2}}{4\ F} \times \dfrac{R_{O_2}\ T_{st}}{V_{ca}} \\ 0 \\ 0 \end{bmatrix}, \tag{16}$$

$$s_1(t) = \lambda_{O_2} - \lambda_{O_{2,ref}}\,.$$

Thus, the derivate of s_1 is:

$$\dot{s_1}(t) = \dot{\lambda}_{O_2} - \dot{\lambda}_{O_{2,ref}} \;\rightarrow \dot{s_1}(t) = \dot{\lambda}_{O_2}\,, \tag{17}$$

where:

$$\dot{\lambda}_{O_2} = \frac{X_{O_{2,in}} \dfrac{1}{1+\Omega_{atm}} . K_{SM,OUT}}{\dfrac{n M_{O_2}}{4F} I_{st}} \left[\dot{x_2} - \frac{\dot{x_4}}{M_{O_2}} - \frac{\dot{x_5}}{M_{N_2}} \right] \tag{18}$$

$$= A \frac{\gamma R_a T_{atm}}{V_{sm}} \left[1 + \left(\left(\frac{x_2}{P_{atm}} \right)^4 - 1 \right) n_{cp}^{-1} \right] W_{cp} + A \left[\frac{\gamma x_2}{x_3} (-x_2 B_{12} + B_{13} + B_{14} x_5 + B_{15} x_4) - \frac{\dot{x_4}}{m_{O_2}} - \frac{\dot{x_5}}{m_{n_2}} \right],$$

in which:

$$A = \frac{X_{O_{2,in}} \frac{1}{1+\Omega_{atm}} . K_{SM,OUT}}{\frac{n M_{O_2}}{4F} I_{st}}, \tag{19}$$

The sliding surface $s_2(t)$ can be expressed as:

$$s_2(t) = W_{cp} - W_{cp,ref}\,.$$

We can write the derivative of s_2 as:

$$\dot{s_2}(t) = \dot{W}_{cp} - \dot{W}_{cp,ref} \;\rightarrow$$
$$\dot{s_2}(t) = [B_{10} + B_{11} x_{02} + 2B_{02} x_1] \dot{x}_1 + [B_{10} + 2B_{20} x_2 + B_{11} x_1] \dot{x}_2 - \dot{W}_{cp,ref}\,. \tag{20}$$

By substituting the relation $\dot{x}_1$ (Eq. (1)) in Eq. (20), and considering $D = [B_{10} + B_{11} x_{02} + 2B_{02} x_1]$, we have:

$$\dot{s_2}(t) = D \times B_1 K_t V_{cm} + [B_{10} + 2B_{20} x_2 + B_{11} x_1] \dot{x}_2 + D \left(- \left[\frac{c_p \times T_{atm}}{n_{cp} \times J_{cp} \times x_1} \times W_{cp} \times \left(\left(\frac{x_2}{P_{atm}} \right)^{B_4} - 1 \right) \right] + (-B_2 x_1 k_t) \right) - \dot{W}_{cp,ref}\,. \tag{21}$$

A. Super twisting algorithm sliding mode controller (ST)

Definition 2. The sliding surface $s_2(t)$ by considering the error as $e = W_{cp} - W_{cp,ref}$ can be defined as follows:

$$s_2(t) = \lambda\, e + \dot{e} = \lambda (W_{cp} - W_{cp,ref}) + (\dot{W}_{cp} - \dot{W}_{cp,ref})\,,$$

where λ is a positive constant.

Theorem 1. If we consider the following control law,

$$u = u_1 + u_2 \tag{22}$$

where

$$u_1 = -k_1 \phi_1(s) + \rho_1(t,x)\,,$$
$$\dot{u}_2 = -k_2 \phi_2(s) + \rho_2(t,x)\,, \tag{23}$$

then the Lyapunov function $L(s) = v^T P\, v$ is strong and robust, and the origin is exactly robust, in which k_1, and k_2 are constant gains.

Proof. The first derivative of ST surface is:

$$\dot{s}(t,x,u) = \frac{\partial}{\partial t} s(t,x) + \frac{\partial}{\partial x} [s(t,x)][f(x) + g(x)u]\,, \tag{24}$$

Taking the second derivative of ST surface results in

$$\ddot{s}(t,x,u) = \frac{\partial}{\partial t} \dot{s}(t,x,u) + \frac{\partial}{\partial x} [\dot{s}(t,x,u)][f(x) + g(x)u] + \frac{\partial}{\partial u} \dot{s}(t,x,u)\dot{u} = \varphi(t,x,u) + \emptyset(t,x,u)\dot{u}\,,$$

where

$$\varphi(t,x,u) = \left[\frac{\partial \dot{s}}{\partial x_1}\ \frac{\partial \dot{s}}{\partial x_2}\frac{\partial \dot{s}}{\partial x_3}\frac{\partial \dot{s}}{\partial x_4}\frac{\partial \dot{s}}{\partial x_5}\frac{\partial \dot{s}}{\partial x_6}\right] \times (f(x) + g(x)u)\,, \quad (25)$$

$$\emptyset(t,x,u) = \frac{\partial}{\partial u}\dot{s}(t,x,u)\,.$$

Thus

$$\dot{s} = \phi_2(t,x) + \gamma_2(t,x)u - \dot{W}_{cp,ref}\,.$$

By considering Eq. (25), One can write:

$$\emptyset(t,x,u) = \frac{\partial}{\partial u}\dot{s}(t,x,u) = \gamma_2(t,x) = D \times B_1 K_1\,,$$

$$\varphi(t,x,u) = \frac{\partial \dot{s}}{\partial x_1}\dot{x}_1 + \frac{\partial \dot{s}}{\partial x_2}\dot{x}_2 + \frac{\partial \dot{s}}{\partial x_3}\dot{x}_3 + \frac{\partial \dot{s}}{\partial x_4}\dot{x}_4 + \frac{\partial \dot{s}}{\partial x_5}\dot{x}_5 + \frac{\partial \dot{s}}{\partial x_6}\dot{x}_6\,.$$

We can write Lyapunov's function as a quadratic form:

$$L(s) = v^T P\, v\,,$$

with

$$A^T P + PA = -Q\,,$$

where $v^{\mathrm{T}} = \Phi^{\mathrm{T}}(s) = [\phi_1(s), u_2]$, in which $\phi_1(s) = |s|^{\frac{1}{2}} sign(s)$, $\phi_2(s) = sign(s)$, P is a symmetric matrix that is positive definite and unique, $A = \begin{bmatrix} -k_1 & 1 \\ -k_2 & 0 \end{bmatrix}$ and $Q = Q^T > 0$ is a positive definite matrix that is equal to its transpose. The controller coefficients have to satisfy the following condition [22] to guarantee finite-time convergence and Lyapunov stability:

$$k_1^2 \geq \frac{4\ g\ d_M(k_2+g)}{d_m^3(k_2-g)}\,, k_2 > \frac{g}{d_m}\,, \quad (26)$$

where for all $u \in U$ and, $x \in X$:we have , $|\frac{\delta}{\delta x}s| \leq g$, $0 < d_m < \frac{\delta}{\delta x}\dot{s} < d_M$.

Fig. 3 shows the super twisting controller (ST) block diagram.

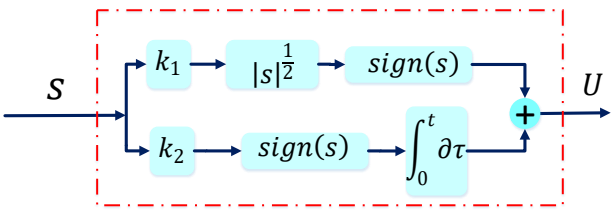

Fig. 3. Block diagram of the ST controller.

A. Variable gain super twisting sliding mode controller

The following expression [31] shows the VGST adaptive control law:

$$u = u_1 + u_2\,, \quad (27)$$

with

$$u_1 = -k_1(t)\phi_1(s) + \rho_1(t,x)\,,$$
$$\dot{u}_2 = -k_2(t)\phi_2(s) + \rho_2(t,x)\,,$$

where $k_1(t)$, and $k_2(t)$ are variable adaptive gains, $\rho_1(t,x)$ and $\rho_2(t,x)$ are perturbations, and $\phi_1(s) = |s|^{\frac{1}{2}} sign(s)$, $\phi_2(s) = sign(s)$. We assume that the perturbations are limited, and they follow these equations:

$$\rho_1(t,x) = r_1(t,x)\phi_1(s)\,, \quad |r_1(t,x)| \leq |c_1(t,x)|,$$
$$\rho_2(t,x) = r_2(t,x)\phi_2(s)\,, \quad |r_2(t,x)| \leq |c_2(t,x)|, \quad (28)$$

where $c_1(t,x) \geq 0$, $c_2(t,x) \geq 0$ are continuous functions that are known. Using Lyapunov stability analysis, we derive the gains of the VGST controller in the next theorem.

Theorem 2. Let the gains of the control law Eq. (27) with the perturbation conditions Eq. (28) be

$$k_1(t,x,s) = \delta + \frac{1}{\beta}\left\{\frac{1}{4\eta}[2\eta c_1 + c_2]^2 + 2\eta c_2 + \eta + [2\eta + c_1(t,x)](\beta + 4\eta^2)\right\}, \quad (29)$$

$$k_2(t,x,s) = \beta + 4\eta^2 + 2\eta k_1(t,x,s)\,.$$

Then:

a) The Lyapunov function $L(s) = v^T P\, v$ is strong and robust, and the origin is exactly robust, where $v^{\mathrm{T}} = \Phi^{\mathrm{T}}(s) = [\phi_1(s), u_2]$, and P is a unique positive definite symmetric matrix.

b) The sliding surface s(t) tends to the origin in the following finite time T:

$$T = \frac{2}{\vartheta_1} L^{\frac{1}{2}}(0) \quad (30)$$

Proof.

a) Let's look at the following quadratic Lyapunov function:

$$L(s) = v^T P\, v\,,$$
$$A^{\mathrm{T}}P + PA = -Q\,, \quad (31)$$

where $A = \begin{bmatrix} -k_1 & 1 \\ -k_2 & 0 \end{bmatrix}$ and $Q = Q^T > 0$ is a symmetric positive definite matrix.

One can write $\phi_2(s) = \phi'_1(s)\phi_1(s)$, and $\phi'_1(s) = \frac{1}{2}|s|^{-\frac{1}{2}}$. Thus

$$\dot{v} = \begin{bmatrix} \phi'_1(s)\{-k_1\,\phi_1(s) + s\} \\ -k_2\,\phi_2(s) \end{bmatrix} = \phi'_1(s) \begin{bmatrix} -k_1, 1 \\ -k_2, 0 \end{bmatrix} v = \phi'_1(s)\, A\, v\,,$$

The derivative of the Lyapunov function is:

$$\dot{L}(s) = \dot{v}^{\mathrm{T}}Pv + v^{\mathrm{T}}P\dot{v} = \phi'_1(s)v^{\mathrm{T}}(A^{\mathrm{T}}P + PA)v = -\phi'_1(s)v^{\mathrm{T}}Qv \quad (32)$$

where Q can be obtained from the equation ALE Eq. (31). From [31], one obtain:

$$|\rho_1(t,x)| \leq k_c|s|^{\frac{1}{2}}c_1(t,x)\,, \quad (33)$$

$$\left|\frac{d}{dt}\rho_2(t,x)\right| \leq \frac{k_c^{\,2}}{2}c_2(t,x)\,. \quad (34)$$

From Eq. (31), we can write:

$$Q(t,x)=\begin{bmatrix}2(k_1(t,)-r_1(t,x))p_1 & * \\ +2(k_2(t,x)-r_2(t,x))p_3 & \\ (k_1(t,x)-r_1(t,x))p_3 & -2p_3 \\ +(k_2(t,x)-r_2(t,x))p_2-p_1 & \end{bmatrix},$$

where * denotes the transpose of the corresponding element below the main diagonal of the matrix Q(t,x). Now, if we consider

$$P=\begin{bmatrix}p_1 & p_3\\ p_3 & p_2\end{bmatrix}=\begin{bmatrix}\beta+4\eta^2 & -2\eta\\ -2\eta & 1\end{bmatrix},$$

then, by substituting p_1, p_2, and p_3 in $Q(t,x)$ and setting $k_2=2\eta k_1+\beta+4\eta^2$.

We have

$$Q-2\eta I=\begin{bmatrix}2\beta k_1+4\eta(2\eta k_1-k_2) & *\\ -2(\beta+4\eta^2)r_1+4\eta r_2-2\eta & \\ k_2-2\eta k_1-(\beta+4\eta^2)+2\eta r_1 & 2\eta\end{bmatrix}$$
$$=\begin{bmatrix}2\beta k_1-(\beta+4\eta^2)(4\eta+2r_1) & *\\ +4\eta r_2-2\eta & \\ 2\eta r_1-r_2 & 2\eta\end{bmatrix},$$

The Q-matrix is positive for all values of (t, x) if:

$$k_1>\frac{2\eta r_2+(\beta+4\eta^2)(2\eta+r_1)+\eta}{\beta}.$$

Now, we need to show that $\dot{L}(s)$ is negative definite. We know that

$$\lambda_{\min}\{P\}\|v\|_2^2\le v^{\mathrm{T}}Pv\le\lambda_{\max}\{P\}\|v\|_2^2,$$

where $\|v\|_2^2=\phi_1^2(s)+u_2^2=|s|+u_2^2$, and note that the inequality $|s|^{-\frac{1}{2}}\le|\phi_1(s)|\le\|v\|_2\le\frac{L^{\frac{1}{2}}(s)}{\lambda_{\min}^{\frac{1}{2}}\{P\}}$ holds.

Therefore, $-|s|^{-\frac{1}{2}}\le-\frac{L^{\frac{1}{2}}(s)}{\lambda_{\min}^{\frac{1}{2}}\{P\}}$. Consequently

$$\dot{L}(s)=-\phi'_1(s)v^{\mathrm{T}}Q(t,x)v\le-2\eta\phi'_1(s)v^{\mathrm{T}}v\le-\vartheta L^{\frac{1}{2}},\quad(35)$$

where

$$\vartheta=\frac{\eta\left(\lambda_{\min}^{\frac{1}{2}}\{P\}\right)^{-1}}{\lambda_{\max}\{P\}}.$$

b) Solving the following differential equation gives the convergence time T:

$$\dot{L}(s)=-\vartheta L^{\frac{1}{2}},\quad L(0)=L_0\ge0.$$

So, we have

$$L(t)=\left(L_0^{\frac{1}{2}}-\frac{1}{2}\vartheta t\right)^2\quad\text{if}\quad\gamma>0.$$

As a result, all system trajectories of Eq. (27) converge in finite time for all perturbations with the following convergence time T:

$$T=\frac{2}{\gamma_1}L^{\frac{1}{2}}(0).$$

Therefore L decreases uniformly and has a stable asymptotic origin. This means that L is a strong Lyapunov function.

To ensure finite-time convergence and to establish Lyapunov stability conditions, the controller coefficients have to be determined as follows [22]:

$$k_1(t,x,s)=\delta+\frac{1}{\beta}\left\{\frac{1}{4\eta}[2\eta c_1+c_2]^2+2\eta c_2+\eta+[2\eta+c_1(t,x)](\beta+4\eta^2)\right\}\quad(36)$$

$$k_2(t,x,s)=\beta+4\eta^2+2\eta k_1(t,x,s),$$

where $\beta>0$, $\eta>0$, and $\delta>0$ are arbitrary positive constants. This completes the proof.

Fig. 4 depicts the variable gain super twisting controller (VGST) controller block diagram.

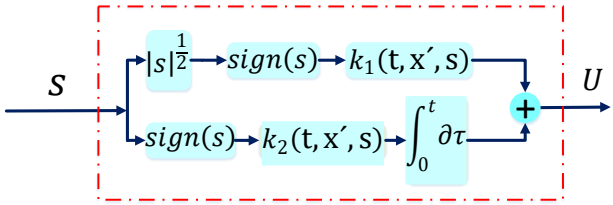

Fig. 4. Block diagram of the VGST controller.

IV. Robust cascade control of fuel cell systems using variable gain sliding mode

Eqs. 1-6. describe the dynamics of the simplified system. A cascade structure is designed using the second order sliding mode control technique, which is shown in the block diagram in Fig. 5. This control method is robust to disturbances and parametric uncertainties.

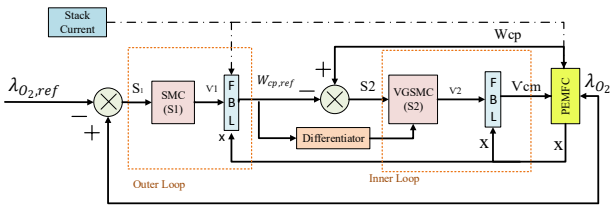

Fig. 5. Schematic of control system with cascade structure.

The control goal is to keep the excess oxygen (λ_{O_2}) at 2.5. The control system has two loops: External loop and internal loop. The External loop uses a second-order sliding mode controller (2-SMC) with a fixed gain super twisting algorithm to control the excess oxygen ratio, which has the excess oxygen error as the input. The controller output, $W_{cp,ref}$, is the target air flow for the compressor. The internal loop uses a feedback controller and variable gain super twisting algorithm to control the compressor air flow, which produces the compressor motor voltage, V_{cm}, to be applied to the fuel cell. Two sliding surfaces are selected to guide λ_{O_2} and W_{cp} to their target values, $\lambda_{O_{2,ref}}$, and $W_{cp,ref}$.

A. External loop

The sliding surface of external loop is defined as follows:

$$s_1(t)=\lambda_{O_2}-\lambda_{O_{2,ref}}.$$

Another way to write Equation (18) is:

$$\dot{s_1} = \dot{\lambda_{O_2}} = \gamma_1 W_{cp} + \phi_1 , \quad (37)$$

where

$$\phi_1(t,x) = A\left[\frac{\gamma x_2}{x_3}(-x_2 B_{12} + B_{13} + B_{14}x_5 + B_{15}x_4) - \frac{\dot{x_4}}{m_{O_2}} - \frac{\dot{x_5}}{m_{n_2}}\right], \quad (38)$$

$$\gamma_1(t,x) = A\frac{\gamma R_a T_{atm}}{V_{sm}}\left[1 + \left(\left(\frac{x_2}{P_{atm}}\right)^4 - 1\right) n_{cp}^{-1}\right] .$$

Using linearization feedback technique, we will have:

$$W_{cp,ref} = \gamma_1(t,x)^{-1}\left(v_1 - \phi_1(t,x)\right) , \quad (39)$$

v_1 results to integral $\dot{s_1} = v_1$ which is designed to stabilize this new system.

$$v_1 = v_{11} + v_{12} ,$$
$$\dot{v_{11}} = -\beta_1 \text{sign}(s_1) ,$$
$$v_{12} = -\alpha_1 |s_1|^{\frac{1}{2}} \text{sign}(s_1) , \quad (40)$$
$$\alpha_1 = -0.5 \ ; \ \beta_1 = 0.5 .$$

α_1, and β_1 are obtained according to the described terms in Eq. (26). For this purpose, the limits of the maximum and minimum values of $\phi_1(t,x)$, $\gamma_1(t,x)$ were obtained by programming with MATLAB based on the limits of system state changes.

B. Internal Loop

The sliding surface $s_2(t)$ can be expressed as:

$$s_2(t) = W_{cp} - W_{cp,ref} .$$

Another way to write Eq. (20) is:

$$\dot{s_2} = \phi_2(t,x) + \gamma_2(t,x)v_{cm} - \dot{W}_{cp,ref} . \quad (41)$$

where

$$\gamma_2(t,x) = \frac{\partial s}{\partial v_{cm}} = D \times B_1 K_1$$
$$\phi_2(t,x) = \frac{\partial s}{\partial x_2}\dot{x}_2 + \frac{\partial s}{\partial x_1}\dot{x}_1 =$$
$$D\left(-\left[\frac{c_p \times T_{atm}}{n_{cp} \times J_{cp} \times x_1} W_{cp}\left(\left(\frac{x_2}{P_{atm}}\right)^{B_4} - 1\right)\right] + (-B_2 x_1 k_t)\right) + [B_{10} + 2B_{20}x_2 + B_{11}x_1]\dot{x_2} . \quad (42)$$

Using linearization feedback technique:

$$v_{cm} = \gamma_2(t,x)^{-1}\left(v_2 - \phi_2(t,x) + \dot{W}_{cp,ref}\right) , \quad (43)$$

where v_2 results to an integrator $\dot{s_2} = v_2$ which is designed to stabilize this new system. V_2 equal to u in Eq. (27).

For obtained perturbation bounds and so v_2, we need to define the sliding variable as a new variable. So, the S variable becomes part of the new set of variables as follows:

$$s_2(t) = W_{cp} - W_{cp,ref} \quad (44)$$

This implies:

$$s_2 = B_{00} + B_{10}(x_2) + B_{20}x_2^2 + B_{10}x_1 + B_{11}x_2x_1 + B_{02}x_1^2 - W_{cp,ref} \quad (45)$$

Therefore, we can compute the new value of x_1 as follows:

$$-s_2 + B_{00} + B_{10}(x_2) + B_{20}x_2^2 + B_{10}x_1 + B_{11}x_2x_1 + B_{02}x_1^2 - W_{cp,ref} = 0 \quad (46)$$

As a result:

$$x_1 = \frac{-(B_{11}x_2 + B_{10})}{2B_{02}} \mp \frac{\sqrt{(B_{11}x_2 + B_{10})^2 + 4B_{02}(s_2 + W_{cp,ref} - B_{00} - B_{10}x_2 - B_{20}x_2^2)}}{2B_{02}} \quad (47)$$

Now, we have a new set of conditions for $x_{new} = \{x_2, x_3, x_4, x_5, x_6\}$. Let $x_1 = a(t, x_{new}, s) = B_{106}\,x_2 - B_{107} \mp \sqrt{B_{104}\,{x_2}^2 + B_{103}\,x_2 + B_{105} + \frac{s_2 + W_{cp,ref}}{B_{02}}}$, now, with substitute the value of $\dot{x_1}$ in the Eq. (21) we have:

$$\dot{W}_{cp} = [B_{10} + B_{11}x_{02} + 2B_{02}a(t, x_{new}, s)]\dot{x}_1 + [B_{10} + 2B_{20}x_2 + B_{11}a(t, x_{new}, s)]\dot{x}_2 \quad (48)$$

Let $D = [B_{10} + B_{11}x_2 + 2B_{02}a(t, x_{new}, s)]$ and substitute the value of $\dot{x_1}$ in the following:

$$\dot{W}_{cp} = D \times B_1 K_1 V_{cm} + D\left(-\left[\frac{c_p \times T_{atm}}{n_{cp} \times J_{cp} \times a(t, x_{new}, s)} \times W_{cp} \times \left(\left(\frac{x_2}{P_{atm}}\right)^{B_4} - 1\right)\right] + (-B_2 a(t, x_{new}, s)k_t)\right) + [B_{10} + 2B_{20}x_2 + B_{11}a(t, x_{new}, s)]\dot{x}_2 . \quad (49)$$

This results in:

$$\dot{s}_2 = f_s(t, x_{new}, s) + g_s(x_{new}, s)V_{cm} , \quad (50)$$

where

$$g_s(x_{new}, s) = \frac{\partial s}{\partial v_{cm}} = D \times B_1 K_1$$
$$f_s(t, x_{new}, s) = \frac{\partial s}{\partial x_2}\dot{x}_2 + \frac{\partial s}{\partial x_1}\dot{x}_1 =$$
$$D\left(-\left[\frac{c_p \times T_{atm}}{n_{cp} \times J_{cp} \times a(t, x_{new}, s)} W_{cp}\left(\left(\frac{x_2}{P_{atm}}\right)^{B_4} - 1\right)\right] + (-B_2 a(t, x_{new}, s)k_t)\right) + [B_{10} + 2B_{20}x_2 + B_{11}a(t, x_{new}, s)]\dot{x_2} - \dot{W}_{cp,ref} . \quad (51)$$

To find the boundaries, we extract the functions $\rho_1(x)$ and $\rho_2(x)$ as follows:

$$\dot{s} = f_s(t, x_{new}, s) + u = \underbrace{f_s(t, x_{new}, 0)}_{\rho_2(t, x_{new})} + \underbrace{[f_s(t, x_{new}, s) - f_s(t, x_{new}, 0)]}_{\rho_1(t, x_{new}, s)} + u ,$$
$$\rho_1(t, x_{new}, s) = D(t, x_{new}, s)\left(-\left[\frac{c_p \times T_{atm}}{n_{cp} \times J_{cp} \times h} W_{cp}\left(\left(\frac{x_2}{P_{atm}}\right)^{B_4} - 1\right)\right] + (-B_2 a(t, x_{new}, s)k_t)\right) + [B_{10} + 2B_{20}x_2 + B_{11}a(t, x_{new}, s)]\dot{x_2} - \dot{W}_{cp,ref} - \rho_2(x_{new}, t) , \quad (52)$$

$$\rho_2(x_{new}, t) = D(t, x_{new}, 0)\left(-\left[\frac{c_p \times T_{atm}}{n_{cp} \times J_{cp} \times h} W_{cp}\left(\left(\frac{x_2}{P_{atm}}\right)^{B_4} - 1\right)\right] + (-B_2 a(t, x_{new}, 0)k_t)\right) + [B_{10} + 2B_{20}x_2 + B_{11}h(t, x_{new}, 0)]\dot{x_2} - \dot{W}_{cp,ref} \quad (53)$$

Then, we obtain $\dot{\rho}_2$ and ρ_1 from the extension of Eq. (51), and we can calculate $c_2(t,x)$, $c_1(t,x)$. Due to the complexity of the equations, these calculations were done by MATLAB software. The proposed control scheme integrates a high-precision robust differentiator for real-time estimation of $\dot{W}_{cp,ref}$Error! Bookmark not defined. [32]. The differentiator implements the following second-order sliding mode algorithm:

$$\begin{cases} \dot{z}_0 = -\gamma_1 L^{\frac{1}{2}}|z_0 - s|^{\frac{1}{2}}\text{sign}(z_0 - s) + z_1 \\ \dot{z}_1 = -\gamma_1 L\,\text{sign}(z_1 - \dot{z}_0) \end{cases} \quad (54)$$

where z_0 is finite-time convergent estimate, z_1 is derivative estimate, γ = [1.10, 1.5] are the fixed gain parameters per [32], and $L > |\ddot{W}_{cp,ref}|$ is the sole tuning parameter (bounded acceleration condition).

V. Results and Discussions

Fig. 6 displays the stack current that acts as a disturbance to the system.

The simulation of the model has been done and then the net power output (P_{net}), the excess oxygen ratio λ_{O_2}, and the compressor flow ratio (W_{cp}) values have been calculated using the equations of the previous section. We used the difference between W_{cp} and $W_{cp,ref}$ as the sliding surface for the controller input. Finally, we obtained the k_1, and k_2 gains and the control system input based on the relations mentioned above. Fig. 7 shows the corresponding simulation in MATLAB environment:

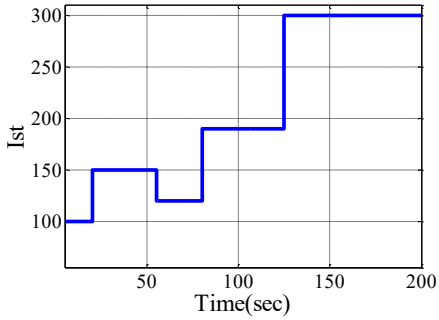

Fig. 6. The load current variation profile as disturbances current

The implementation details of the model and control system simulation in MATLAB are illustrated in Fig. 8. Fig. 9 displays the system states under the variable gain conditions. We can see from the Fig. 9 that the state x_1 or the engine angular velocity, varies between 7000 and 15000 rad/sec, which is a reasonable range. The air mass in the supply manifold changes between 0.03 and 0.06 kg depending on the load current value. The pressure values of the states x_2, x_4, x_5 and x_6 are within the acceptable pressure limits, which indicates that the state control is effective. According to Fig. 10 the compressor voltage or the control input ranges from 100 to 350V. To validate the performance of the cascade controller with variable gain, this controller has been compared with three other controllers, i.e. single loop constant gain ($ST_{C\text{-}loop}$), single loop variable gain ($VGST_{C\text{-}loop}$) and cascaded constant gain ($ST_{Cascade}$). It is also clear from the Fig. 10 that the compressor voltage has much less fluctuations in the conditions of using the cascaded variable gain controller and the cascaded variable gain controller shows better performance than other controllers. The variable gains k_1 and k_2 are shown in Fig. 11 and we can see from the figure that $5 < k_1 < 25$, and $2 < k_2 < 6$.

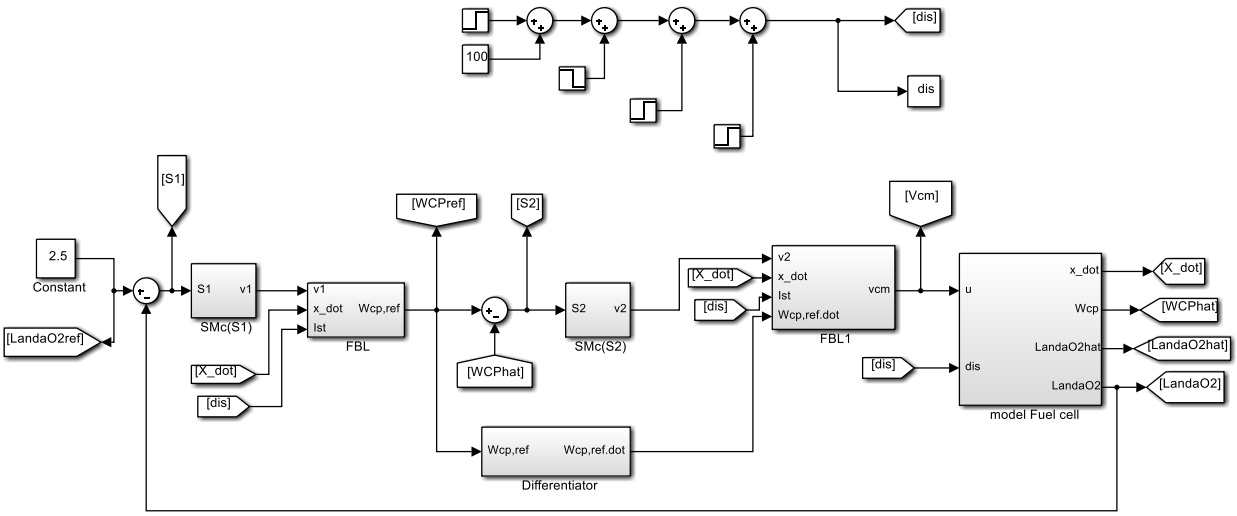

Fig. 7. Block diagram of the control system in Matlab/Simulink environment

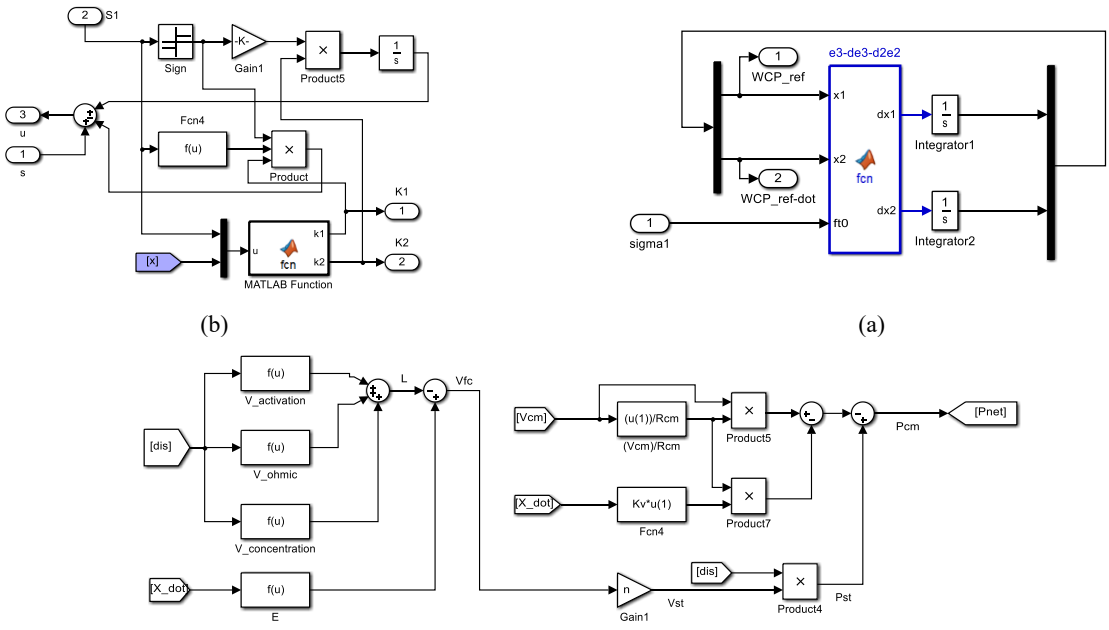

Fig. 8. Simulation framework detailing (a) Levant differentiator implementation, (b) variable-gain control logic with real-time adaptation, and (c) power calculation blocks.

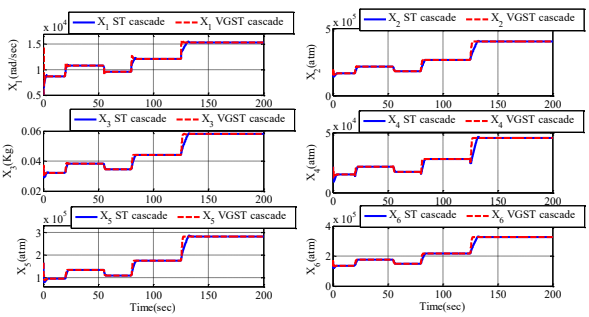

Fig. 9. System States Under Variable vs. Constant Gain Control

Fig. 12 shows the excess oxygen ratio for different controllers. As it is clear from the Fig. 12, the cascade structure variable gain controller performs better than the other three controllers.

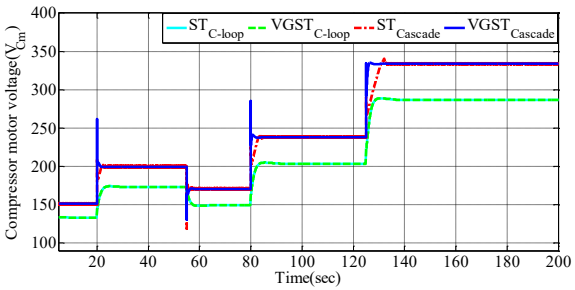

Fig. 10. Compressor voltage and performance comparison of cascade variable-gain vs. constant-gain/single-loop controllers

Fig. 13 shows a comparison between the net output power in the variable gain second-order sliding mode and the constant gain mode in statuses cascade and single close loop.

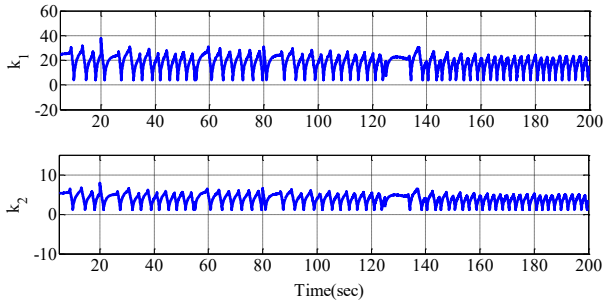

Fig. 11. Variable gains

We can infer from this Fig. 13 that the net output power is higher in the cascade variable gain mode and also, the fuel cell produces a power of about 60 KW at the maximum current. Therefore, there is a significant saving in the total power. Fig. 13 clearly proves the superiority of the variable gain controller of the cascade structure compared to the other three controllers, so that the maximum power value in the cascade variable gain mode is about 10 kW compared to the single loop variable gain and compared to the constant gain mode (single loop and cascade) is about 20 kW more. Fig. 13 in the zoomed mode shows a significant reduction in chattering and a high convergence speed in the variable gain mode, which have better performance in both the cascade mode and the single loop mode compared to the constant gain controllers. Fig. 14 shows the compressor airflow in both cases of applying fixed-gain sliding mode control and variable-gain sliding mode control, and indicates that the proposed cascade variable-gain controller reduces chattering.

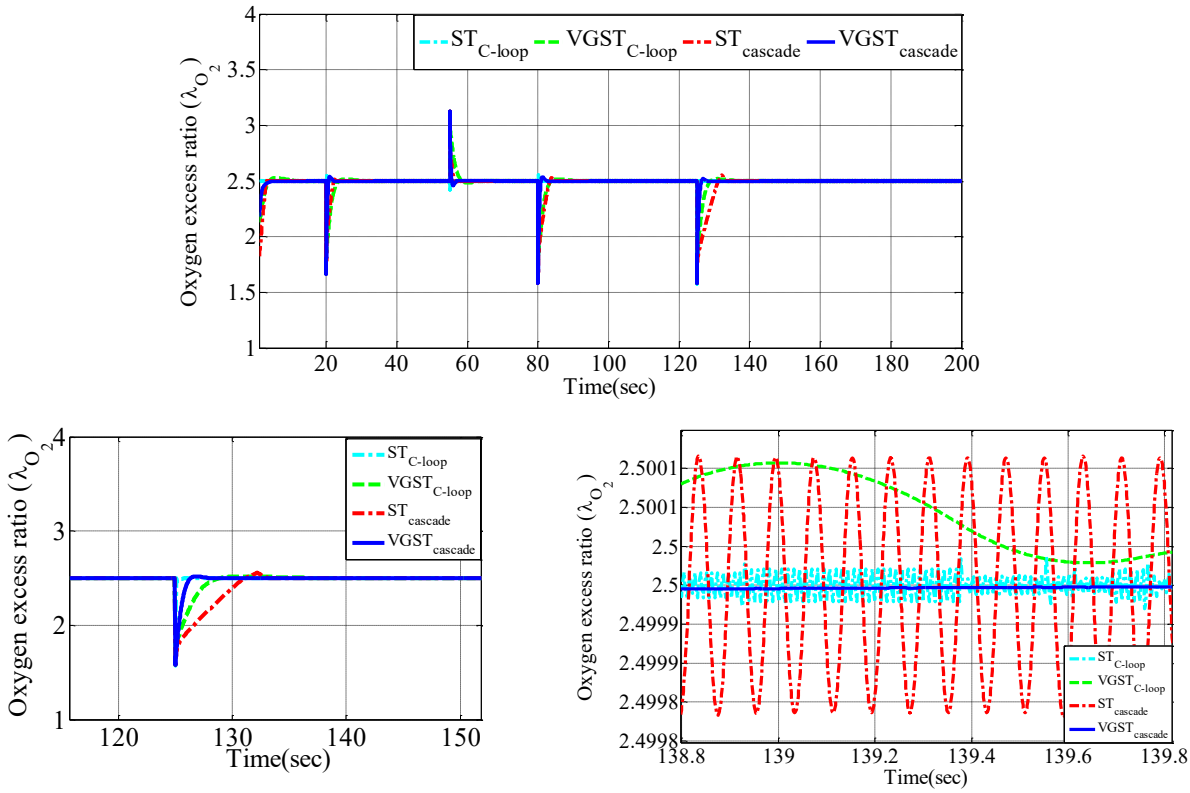

Fig. 12. Excess oxygen ratio under four controllers, demonstrating superior performance of the cascade variable-gain structure.

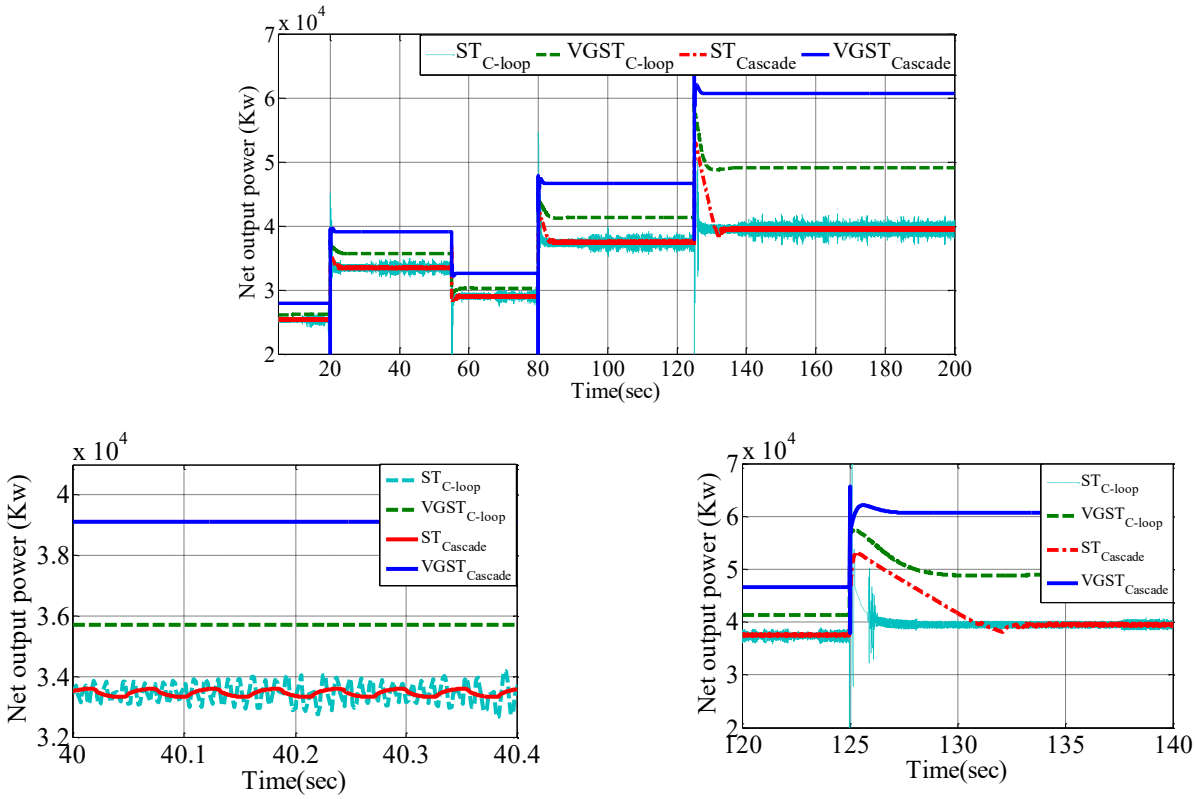

Fig. 13. Net output power comparison of variable-gain vs. constant-gain second-order sliding mode controllers in cascade/single-loop configurations.

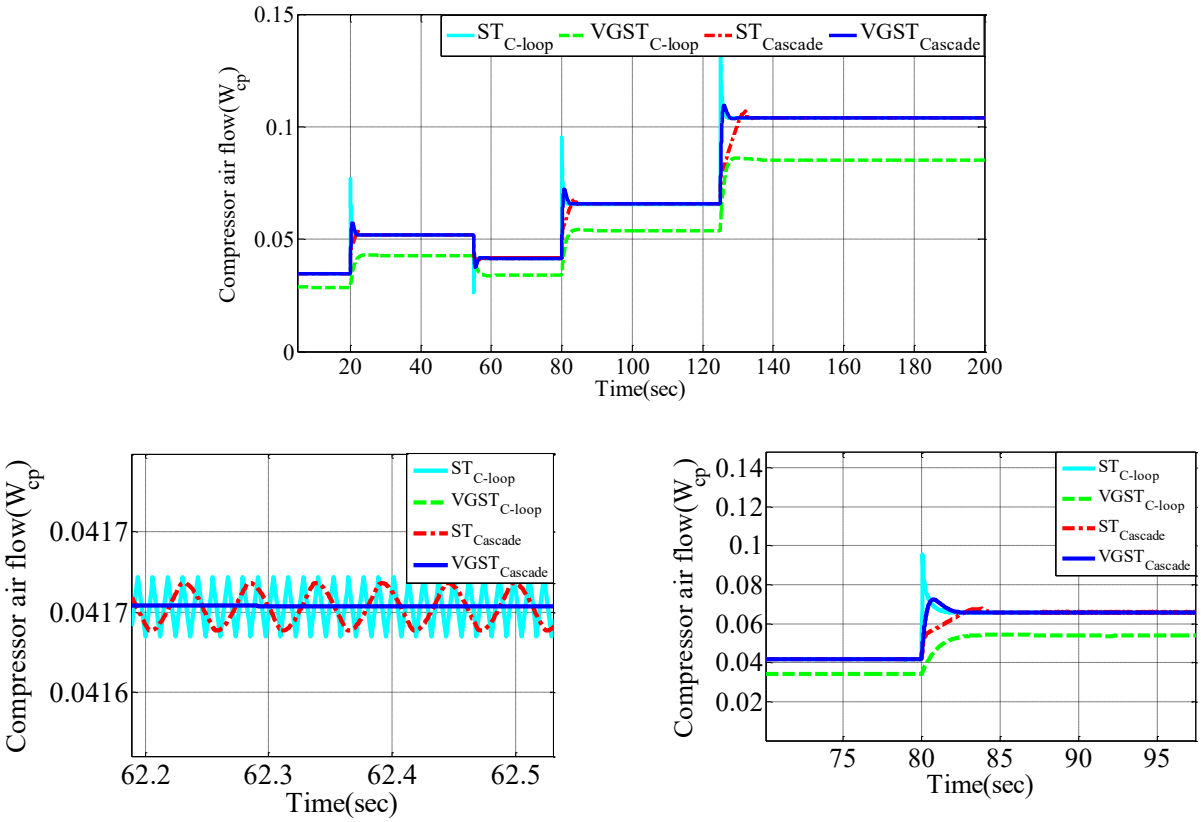

Fig. 14. Compressor airflow comparison: Fixed-gain vs. variable-gain sliding mode control

A. Variations of System Parameters

The parameters of the PEMFC system are difficult to estimate precisely in real conditions. This is because they depend on the environmental factors (e.g., temperature, pressure) and the structural features (e.g., manifolds volumes, rotor inertia, motor resistance, motor inductance, etc.). Sensitivity analysis to model uncertainties was conducted by varying key parameters following Table 2. The controller's robustness was evaluated under parametric variations.

Table 2. Parameter variations applied to simulate model uncertainty and assess controller robustness [22]

parameters	Volatility and uncertainty
Temperature of the stack(T_{st})	+10%
Single stack cathode (V_{ca}) volume	+5%
Motor constant(k_v)	-10%
Electrical resistance of (R_{cm}) motor	+5%
Diameter Compressor(d_c)	+10%
Motor inertia(J_{cp})	+10%
Atmospheric pressure(P_{atm})	+10%
Supply manifold volume(V_{sm})	-10%
Return manifold volume(V_{rm})	-10%

The resulting performance degradation is shown in Fig. 15, and Fig. 16. Fig. 15 is depicted under parametric uncertainty conditions and shows the desired performance of net output power that is between 25 and 50 Kw. It also implies that the closed-loop system is robust against severe parametric uncertainty. Fig. 16 shows that the excess oxygen ratio remains at a value of 2.5 even under conditions of parametric uncertainty. The Fig. 15 and Fig. 16 indicates that the proposed controller effectively handles parametric uncertainty. According to Fig. 17 the compressor voltage or the control input ranges from 100 to 300V. As evident from Fig. 17, the compressor voltage (or controller input) remains bounded despite applied parametric uncertainties and step disturbances (stack current (I_{st})). This demonstrates the system's robustness and the satisfactory performance of the VGST controller.

B. The Noisy Conditions

To evaluate the performance of the proposed controller, Rakhtala et al. [27] have conducted some tests with realistic measurement noise. They also have used the Data Acquisition Card (DAQ) of Advantech USB-4711A as a real application with the LabViewTM to match the simulation data and tests with the experimental system, and have utilized the MatlabTM for extracting the features of the

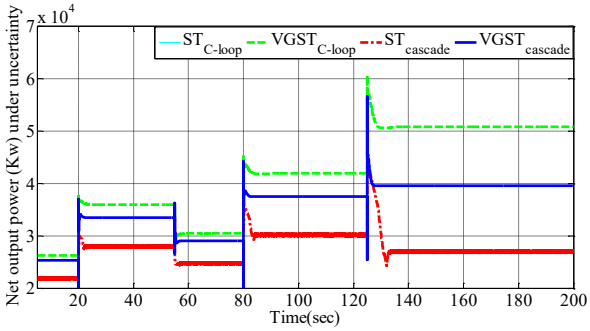

Fig. 15. Robust net output power (25–50 kW) under severe parametric uncertainty.

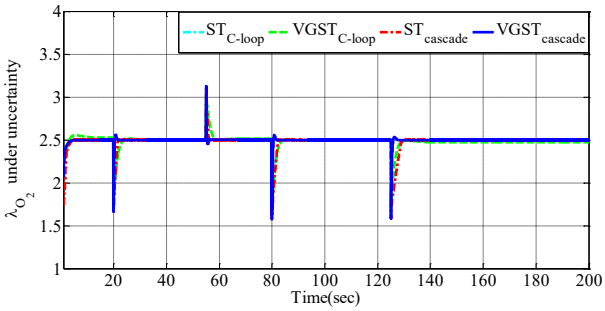

Fig. 16. Robust regulation of excess oxygen ratio (λ_{O_2} = 2.5) under parametric uncertainty

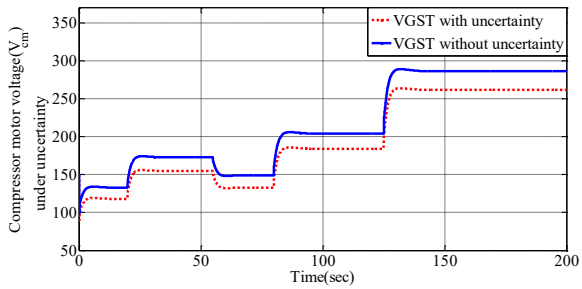

Fig. 17. Compressor voltage (100–300 kW) under severe parametric uncertainty.

measured noise, which are as follows:

Mean=0.0023	Variance=0.13362	Co-variance = 0.0179
PSD=0.22	Signal/noise(SNR)=28dB	Distribution: Gaussian

We added similar noise to the measured signals of the compressor output flow (W_{cp}), which passed through a 2nd-order Butterworth low pass filter with a cut off frequency of 30Hz. The implementation details of the noise generation and injection simulation in MATLAB are illustrated in Fig. 18.

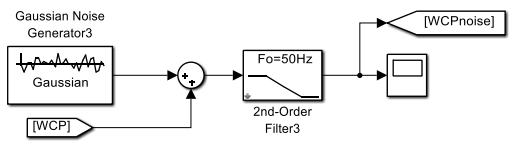

Fig. 18. Simulink block diagram for noise generation and injection.

Fig. 19, Fig. 20, and Fig. 21 show the results of the controlled output under the noisy conditions. One can see from the figures that the control achieved good convergence within a limited time and followed the desired value. Even with the noise, the proposed controller reached the desired value of 2.5, showing a satisfactory tracking and behavior. The net output power also increased in the noisy mode. As evident from Fig. 20, the system states remain bounded under applied noise and step disturbances (stack current (I_{st})), demonstrating the system's robustness and the effective performance of the variable-gain controller.

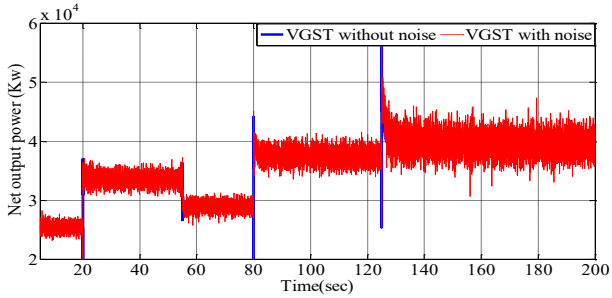

Fig. 19. Net power output under realistic noise condition

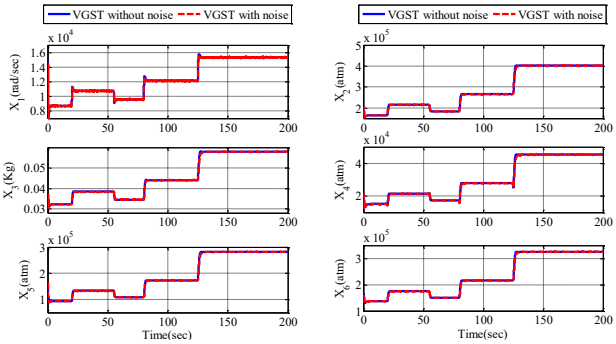

Fig. 20. States profile in the case of variable gain controller under realistic noise condition

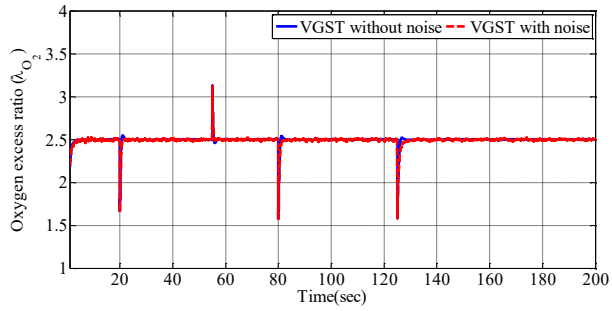

Fig. 21. Oxygen excess ratio under realistic noise condition

The performance of the controllers has been compared from a statistical point view. In this regard, we have used four famous statistical indices: mean square error (MSE), the root-mean-square error (RMS), mean absolute error (MAE), and standard deviation (Sd). To better understand, we have depicted the value of the statistical indices for the error of oxygen excess ratio. As can be seen from Fig. 22, the VGST_Cascade controller has a better performance than the

other controllers because it has the smallest mentioned statistical indices.

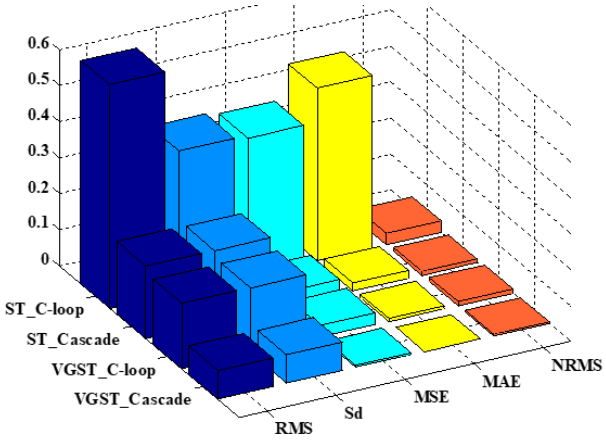

Fig. 22. Comparative evaluation of controller performance using statistical error indices (MSE, RMSE, MAE, SD) for oxygen excess ratio

For better comparison of statistical metrics, the data from Fig. 22 have been tabulated in Table 3.

Table 3. Comparative evaluation of controller performance using statistical error indices for oxygen excess ratio

	RMS	sd	MSE	MAE	NRMS
ST_C-loop	0.520	0.3931	0.3845	0.4795	0.0328
ST_Cascade	0.202	0.2003	0.0406	0.0226	0.011
VGST_C-loop	0.181	0.181	0.0328	0.0089	0.0105
VGST_Cascade	0.079	0.0793	0.0063	4.32E-04	0.0045

Table 4 benchmarks our method against published results for MPC and PID [33].

Table 4. RMS, MSE, and MAE of controllers.

	Error Integral Criterion		
	RMS	**MSE**	**MAE**
VGST_C-loop	0.1812	0.0328	0.0089
VGST_Cascade	0.0793	0.0063	4.32E-04
PID	0.114	0.013	0.0091
MPC	0.190	0.0363	0.046

VI. Conclusion

This paper presents a cascade variable gain super-twisting second-order sliding mode control for the air-feed system of the PEM fuel cell. The PEMFC model is nonlinear and has 6 states, which is adequate for the controller design. The controller was designed using Lyapunov theory and tested using simulation and experimental methods. Also, for further validation, uncertainty and noise in the system were considered and the results were confirmed. Finally, it was shown that the proposed controller performs better and more accurately than the constant gain and closed loop controller. This design method reduces the online calculations by avoiding the computation of chaos and confusion for the controller design and operation. The controller tracks the oxygen stoichiometry precisely and improves the net power output. For the maximum current condition (300A), the net power output is 60 KW, which is 20 KW higher than the constant gain controller. The controller also has the advantages of being robust to noise and uncertainty, reducing chattering, being easy to implement, and having a short convergence time. While VGST exhibits minor tracking errors and strong robustness, its computational load, chattering at UHF, and model dependency remain inherent trade-offs. These are offset by its unique capability to prevent oxygen starvation –a critical safety requirement in PEMFC systems. Future research will extend this controller to hydrogen flow regulation and thermal dynamics integration, enhancing operational stability under load transients. Additionally, hybrid fuel cell-battery system implementation will be explored to optimize power management. These extensions address critical limitations while advancing toward real-world multi-physics control solutions.

Appendix A:

Table 5. Value of parameters [22].

Symbol	Parameter	Value
P_{atm}	Atmospheric pressure (Pa)	101.325
$P_{sat,Tatm}$	Saturation pressure in ambient temperature (Pa)	3.14×10^{3}
$P_{sat,Tst}$	Saturation pressure in stack temperature (Pa)	4.09×10^{4}
$\emptyset_{atm}$	Average ambient air relative humidity	0.5
$\emptyset_{ca,in}^{des}$	Relative humidity in cathode inlet	1
T_{atm}	Atmospheric temperature (K)	298.15
γ	Air-specific heat ratio	1.4
C_p	Air density (J/kg/K)	1004
R	Universal gas constant (J/mol/K)	8.31
ρ_a	Air density (kg/m^3)	1.23
R_a	Air gas constant (J/mol/K)	286.9
R_{O_2}	Oxygen gas constant (J/kg/K)	259.8
R_{N_2}	Nitrogen gas constant (J/kg/K)	296.8
R_v	Vapor gas constant (J/kg/K)	461.5
Ma	Molar mass of air (kg/mol)	28.9×10^{-3}
M_{o_2}	Molar mass of oxygen (kg/mol)	30×10^{-3}
M_{n_2}	Molar mass of nitrogen (kg/mol)	28×10^{-3}
Mv	Molar mass of vapor (kg/mol)	18.0×10^{-3}
$m_{v,ca,max}$	Maximum molar mass of vapor in cathode (kg/mol)	3×10^{-3}
F	Faraday's constant (C/mol)	96,487
T_{st}	Temperature of the stack (K)	353
Kt	Motor constant (N m/A)	0.0153
Rcm	Motor constant (ohm)	0.82
Kv	Motor constant (V/(rad/s))	0.0153

η_{cp}	Compressor efficiency	0.8
η_{cm}	Compressor motor mechanical efficiency	0.98
n	Number of cells in fuel cell stack	381
A_{fc}	Fuel cell active area (m^2)	280×10^{-4}
V_{sm}	Supply manifold volume (m^3)	0.02
V_{ca}	Single stack cathode volume (m^3)	0.005
V_{rm}	Return manifold volume (m^3)	0.005
$K_{\mathrm{sm,out}}$	Supply manifold outlet orifice constant (kg/s/Pa)	0.363×10^{-5}
$K_{\mathrm{c\,a,out}}$	Cathode outlet orifice constant (kg/s/Pa)	0.22×10^{-5}
dc	Compressor diameter (m)	0.2286
$y_{\mathrm{O_2,in}}$	Oxygen mole fraction at cathode inlet	0.21

References

[1] J. Kuang, J. Lv, W. Hao, X. Lin, D. Zhao, I. Matraji*, et al.*, "Oxygen excess ratio control of PEM fuel cell systems with prescribed regulation time," *ISA transactions,* vol. 142, pp. 683-692, 2023.

[2] R. Y. Dahham, H. Wei, and J. Pan, "Improving thermal efficiency of internal combustion engines: recent progress and remaining challenges," Energies, vol. 15, p. 6222, 2022.

[3] D. Wu, C. Peng, C. Yin, and H. Tang, "Review of system integration and control of proton exchange membrane fuel cells," Electrochemical Energy Reviews, vol. 3, pp. 466-505, 2020.

[4] Q. Li, W. Yang, L. Yin, and W. Chen, "Real-time implementation of maximum net power strategy based on sliding mode variable structure control for proton-exchange membrane fuel cell system," IEEE Transactions on Transportation Electrification, vol. 6, pp. 288-297, 2020.

[5] C. R. d. Aguiar, K. M. d. Aguiar, R. F. Bastos, W. C. Leal, M. O. Godinho, G. H. Fuzato, et al., "Energy management and operation control of fuel cells in grid-tied operation," Journal of Control, Automation and Electrical Systems, pp. 1-12, 2021.

[6] Y. Nagao, "Proton-Conducting Polymers: Key to Next-Generation Fuel Cells, Electrolyzers, Batteries, Actuators, and Sensors," ChemElectroChem, p. e202300846, 2024.

[7] A. Tang, L. Yang, T. Zeng, and Q. Yu, "Cascade Control Method of Sliding Mode and PID for PEMFC Air Supply System," Energies, vol. 16, p. 228, 2022.

[8] Y. Mousavi, G. Bevan, I. B. Kucukdemiral, and A. Fekih, "Sliding mode control of wind energy conversion systems: Trends and applications," Renewable and Sustainable Energy Reviews, vol. 167, p. 112734, 2022.

[9] K. R. Palepogu and S. Mahapatra, "Design of sliding mode control with state varying gains for a Benchmark Twin Rotor MIMO System in Horizontal Motion," European Journal of Control, vol. 75, p. 100909, 2024.

[10] M. Ebrahimipour and S. M. Mirhosseini-Alizamini, "Optimal Adaptive Sliding Mode Control for a Class of Nonlinear Affine Systems," Control and Optimization in Applied Mathematics, vol. 9, pp. 123-138, 2024.

[11] M. Ghamgosar, S. M. Mirhosseini-Alizamini, and M. Dadkhah, "Design of optimal sliding mode control based on linear matrix inequality for fractional time-varying delay systems," International Journal of Industrial Electronics Control and Optimization, vol. 5, pp. 317-325, 2022.

[12] M. Gholami, S. Mirhosseini-Alizamini, and A. Heidari, "Designing a sliding mode controller for a class of multi-controller COVID-19 disease model," Iranian Journal of Numerical Analysis and Optimization, vol. 15, pp. 27-53, 2025.

[13] G. Khaledi, S. M. Mirhosseini-Alizamini, and S. Khaleghizadeh, "Sliding mode control design for a class of uncertain time-delay conic nonlinear systems," Iranian Journal of Science and Technology, Transactions A: Science, vol. 46, pp. 583-593, 2022.

[14] A. Rezaie, "Sliding Mode Control for Chaotic Systems with Unknown Uncertainties," International Journal of Industrial Electronics Control and Optimization, vol. 7, pp. 53-60, 2024.

[15] F. Roshanravan and A. Heydari, "Sliding Mode Control Design for a Class of Nonlinear Fractional Systems with Application to Glucose-Insulin Systems," International Journal of Industrial Electronics Control and Optimization, vol. 5, pp. 337-347, 2022.

[16] G. R. Shahabadi and M. R. Naseh, "Novel Sliding Mode Control Approach for Quasi-Z-Source Converters with Improved Performance," International Journal of Industrial Electronics Control and Optimization, vol. 7, pp. 213-224, 2024.

[17] T. Gonzalez, J. Moreno, and L. Fridman, "Variable gain super-twisting sliding mode control," Automatic Control, IEEE Transactions on, vol. 57, pp. 2100-2105, 2012.

[18] F. Chen, J. Jiao, Z. Hou, W. Cheng, J. Cai, Z. Xia, et al., "Robust polymer electrolyte membrane fuel cell temperature tracking control based on cascade internal model control," Journal of Power Sources, vol. 479, p. 229008, 2020.

[19] S. Kart, F. Demir, İ. Kocaarslan, and N. Genc, "Increasing PEM fuel cell performance via fuzzy-logic controlled cascaded DC-DC boost converter," International Journal of Hydrogen Energy, vol. 54, pp. 84-95, 2024.

[20] Y. Du, Y. Zhang, J. Lou, J. Wang, and P. Zhao, "Conception and thermo-economic performance investigation of a novel solid oxide fuel cell/gas turbine/Kalina cycle cascade system using ammonia-water as fuel," Applied Thermal Engineering, vol. 239, p. 122118, 2024.

[21] H. Luo, J. Xiao, P. Bénard, C. Yuan, L. Tong, R. Chahine, et al., "Thermodynamic modeling and analysis of cascade hydrogen refuelling with three-stage pressure and temperature for heavy-duty fuel cell vehicles," International Journal of Hydrogen Energy, vol. 63, pp. 103-113, 2024.

[22] N. Mirrashid, S. M. Rakhtala, and M. Ghanbari, "Robust control design for air breathing proton exchange membrane fuel cell system via variable gain second-order sliding mode," Energy Science & Engineering, vol. 6, pp. 126-143, 2018.

[23] N. Mirrashid, E. Alibeiki, and S. M. Rakhtala, "Nonlinear robust controller design for an upper limb rehabilitation robot via variable gain super twisting sliding mode," International Journal of Dynamics and Control, vol. 10, pp. 1996-2010, 2022.

[24] G. P. Incremona, M. Rubagotti, M. Tanelli, and A. Ferrara, "A general framework for switched and variable gain higher order sliding mode control," IEEE Transactions on Automatic Control, vol. 66, pp. 1718-1724, 2020.

[25] R. Ma, Y. Han, and W. Pan, "Variable-gain super-twisting sliding mode damping control of series-compensated

DFIG-based wind power system for SSCI mitigation," Energies, vol. 14, p. 382, 2021.
[26] J. J. Moré, P. F. Puleston, E. Fossas, and C. Kunusch, "Decoupled inputs sliding mode controllers for a fuel cell-supercapacitor module in hybrid generation applications," International Journal of Energy and Environmental Engineering, vol. 10, pp. 257-269, 2019.
[27] S. M. Rakhtala, A. R. Noei, R. Ghaderi, and E. Usai, "Design of finite-time high-order sliding mode state observer: A practical insight to PEM fuel cell system," Journal of Process Control, vol. 24, pp. 203-224, 2014.
[28] S. M. RakhtAla and R. Eini, "Nonlinear modeling of a PEM fuel cell system; a practical study with experimental validation," arXiv preprint arXiv:2501.08420, 2025.
[29] X. Tang, M. Yang, L. Shi, Z. Hou, S. Xu, and C. Sun, "Adaptive state-of-health temperature sensitivity characteristics for durability improvement of PEM fuel cells," Chemical Engineering Journal, vol. 491, p. 151951, 2024.
[30] T. L. Oladosu, J. Pasupuleti, T. S. Kiong, S. P. J. Koh, and T. Yusaf, "Energy management strategies, control systems, and artificial intelligence-based algorithms development for hydrogen fuel cell-powered vehicles: A review," International Journal of Hydrogen Energy, vol. 61, pp. 1380-1404, 2024.
[31] H. Obeid, S. Laghrouche, L. Fridman, Y. Chitour, and M. Harmouche, "Barrier function-based adaptive super-twisting controller," IEEE Transactions on Automatic Control, vol. 65, pp. 4928-4933, 2020.
[32] A. Levant, "Robust exact filtering differentiators," European Journal of Control, pp. 6-29, 2019.
[33] Y. Wang, H. Li, H. Feng, K. Han, S. He, and M. Gao, "Simulation study on the PEMFC oxygen starvation based on the coupling algorithm of model predictive control and PID," Energy Conversion and Management, vol. 249, p. 114851, 2021.

Violet Farhad received his B.S. degree in Applied Mathematics from Mazandaran University, Babolsar in 1996, her M.S. degree in Applied Mathematics from Islamic Azad University ,Karaj in 2001. She is currently a PhD candidate in Applied Mathematics (Control & Optimization) from PNU, Tehran, Iran. Her current research interests include Advanced Cotrol Systems, Cascade Control Design, Fuel Cell Systems (PEMFC), Optimal and Nonlinear Control Methods, Applied Mathematics in Control Engineering, Higher Education and Interdisciplinary Research.

Seyed Mehdi Mirhosseini-Alizamini received his b.s. Degree in applied Mathematics from damghan university, damghan in 2004, his m.s. Degree in appiled mathematics (control & optimization) from isfahan university of technology, isfahan in 2006, and his ph.d. In applied mathematics (control & optimization) from pnu, tehran in 2015 under the supervision of professor sohrab effati at the ferdowsi university of mashhad, mashhad, iran. Currently he is an associate professor at department of mathematics of payame noor university, iran.his research interests are time daily systems, optimal control, fractional optimal control problems and numerical methods